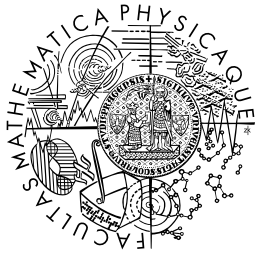

FACULTY
OF MATHEMATICS
AND PHYSICS
Charles University

BACHELOR THESIS

Vojtěch Pařízek

Simulations of the magnetic domains dynamics in antiferromagnetic CuMnAs

Department of Chemical Physics and Optics

Supervisor of the bachelor thesis: prof. RNDr. Petr Němec, Ph.D.
Consultant of the bachelor thesis: Ing. Jakub Železný, PhD.
Study programme: Physics (B0533A110001)
Study branch: FP (0533RA110001)

Prague 2023

I declare that I carried out this bachelor thesis independently, and only with the cited sources, literature and other professional sources. It has not been used to obtain another or the same degree.

I understand that my work relates to the rights and obligations under the Act No. 121/2000 Sb., the Copyright Act, as amended, in particular the fact that the Charles University has the right to conclude a license agreement on the use of this work as a school work pursuant to Section 60 subsection 1 of the Copyright Act.

In ..... date ....

Author's signature

Dedication. Above all, I would like to thank my consultant Ing. Jakub Železný, PhD. for his guidance and invaluable insights. I am grateful to my supervisor, prof. RNDr. Petr Němec, PhD. for his help. Also, I am thankful to my girlfriend, family and friends for supporting me in my studies.

Title: Simulations of the magnetic domains dynamics in antiferromagnetic CuMnAs

Author: Vojtěch Pařízek

Department: Department of Chemical Physics and Optics

Supervisor: prof. RNDr. Petr Němec, Ph.D., Department of Chemical Physics and Optics

Consultant: Ing. Jakub Železný, PhD.

Abstract: Antiferromagnetic materials are promising materials for implementation in spintronic memory devices. In contrast to the more well-known ferromagnetic materials, which are already used in magnetoresistive random access memory (MRAM) devices, they possess multiple advantages, such as no net magnetization and ultrafast dynamics. Antiferromagnetic memories store information through the orientation of the antiferromagnetic ordering. The magnetoresistance of the materials could be used for the electrical readout of the antiferromagnetic structure. In recent experiments in an antiferromagnet CuMnAs after applying a series of electrical or optical pulses, a change in resistivity associated with a significant decrease in the size of antiferromagnetic domains was observed. This means that one is able to perform electrical or optical writing in antiferromagnets. The state persists for timescales that exceed the magnetic dynamics timescales by many orders of magnitude. Here, we present the findings of the antiferromagnetic domain dynamics simulations in CuMnAs, specifically focusing on the process of small domain relaxation leading to the formation of larger domains. The simulations were based on atomistic spin dynamics. For all temperatures, a growth of magnetic domains was detected. However, the size of the antiferromagnetic domains in the simulations was substantially greater than that observed in the experiments. This suggests that the metastability of nano-fragmented domains is caused by factors which are absent in the simulations. These unknown factors might include defects or impurities of the sample. Since some physical parameters (damping parameter and anisotropy strength) are not experimentally measured, it was needed to find the best-fitting values of those parameters for the following simulations.

Keywords: atomistic spin simulations, magnetic domains, CuMnAs, antiferromagnet

Contents

1. Introduction

Some materials exhibit magnetic order, which can occur in different forms. The classification of magnetic materials is based on the arrangement of their magnetic moments, with ferromagnets being the most commonly utilized type. Ferromagnets are defined as materials that, even in zero external field, have non-zero magnetization. On an atomic level, ferromagnetic moments align parallel to each other, and their vectors have the same direction. This order is long-range. It spans on much larger scales than the crystal lattice. Because ferromagnetic moments are aligned in the same direction, their vector sum is non-zero. A notable characteristic of ferromagnets is their large magnetic permeability.

Antiferromagnets, another kind of magnetic material, have the property of zero net magnetic moment. In antiferromagnets, the magnetic moments of neighbouring atoms are typically aligned in opposite directions. However, this is not always the case, as some antiferromagnets exhibit a more complex ordering of magnetic moments.[7]

It is convenient to define a Néel vector for (two sublattices) antiferromagnets:

$$\boldsymbol{L} = \boldsymbol{M}_A - \boldsymbol{M}_B \tag{1.1}$$

Where $\boldsymbol{M}_A$ and $\boldsymbol{M}_B$ denotes the magnetic moment of atoms in one unit lattice. The area in which magnetic moments, resp. Néel vectors are of the same direction is called ferromagnetic resp. antiferromagnetic domain. There usually are multiple magnetic domains in the material. Ferromagnetic domains can be controlled by an external magnetic field.

In recent years there has been a rise in interest in the topic of antiferromagnets. For a long time, they were somewhat overlooked because the magnetic order of ferromagnetic materials is easier to manipulate and measure. Additionally, there has been no apparent application for antiferromagnets. This was arguably the main reason why antiferromagnets did not receive much attention. However, their ultrafast dynamics, insensitivity to external magnetic fields and possible use in neuromorphic computing motivated scientists to lead further research in the area of antiferromagnetism. This raised the question, of whether antiferromagnets could be the next material to be used in memory devices.

A widely used memory devices based on ferromagnets are hard disk drives (HDDs). HDDs are composed of rotating magnetic platter, in which information is stored in the form of the direction of magnetization of certain regions. In early HDDs, the magnetic-field-based reading method was utilized. This method is executed by positioning the reading head in close proximity to the magnetized platter. The magnetic field induces an electric current, the direction of which is then utilized for the purpose of reading. However, a more efficient reading method involves analyzing the resistivity of an electric current rather than relying on a magnetic field. Modern HDDs utilize the tunnelling magnetoresistance effect to achieve optimal reading performance. Tunnelling magnetoresistance occurs in Magnetic tunnel junctions. Magnetic tunnel junction consists of two layers of ferromagnets separated by an insulator. When an electric current flows through the junction, electrons tunnel through the insulator due to the quantum tunnelling phenomenon. The amplitude of the electric current sensitively depends

on the relative orientation of the magnetization of ferromagnetic layers.[8] The state of the junction can thus be detected by measuring the resistance of the tunnel junction.

Using ferromagnetic spin transport electronics (spintronics) reading of information by electric currents was achieved in memory devices such as MRAM, an abbreviation for magnetic random access memory. MRAMs work on nanosecond time-scales. [18] These devices use magnetic tunnel junctions for the storage of information. This technique eliminates the need for induction coils, which rely on magnetic fields to facilitate reading.

Current generation of MRAMs uses spin transfer torque for writing and tunnel magnetoresistance for reading. Spin-transfer torque is based on the transfer of spins between the two magnetic layers due to a spin-polarized current. In spin polarized current, number of electrons with spin $+\frac{1}{2}$ varies from the number of electrons with spin $-\frac{1}{2}$. Spin polarization of currents is achieved by running an unpolarized current through a layer with fixed magnetic orientation. The spin-polarized current then passes through the other layer, whose orientation can easily be rotated, which switches its magnetization. The first layer is denoted as the fixed layer, and the second one as the free layer.[13]

In ferromagnetic materials, spin-transfer-torque has been utilized for writing and tunnel magnetoresistance (TMR) for reading, prompting researchers to investigate comparable techniques in antiferromagnetic materials. The magnetic orientation of layers in antiferromagnets could be utilized as memory cells, and writing would be possible on the picosecond time scales. Recently, it has been demonstrated that certain antiferromagnetic materials exhibit anisotropic magnetoresistance (AMR), which enables the measurement of antiferromagnetic order.[16] Anisotropic magnetoresistance is the dependence of resistivity on the orientation of magnetic moments with respect to the current and the crystal.[18] Furthermore, the presence of antiferromagnetic switching by electric current in CuMnAs has been detected, indicating its usefulness for writing purposes[18]. Later this effect was also observed in other antiferromagnets.[6] These findings highlight the potential of antiferromagnetic materials for novel spintronic applications

1.1 Experiments in CuMnAs

It was observed that AMR is present in some antiferromagnets[16]. This would allow for magnetization readout. [18] showed that switching an antiferromagnet CuMnAs with the use of spin-orbit torques is possible. In this experiment, a change in the resistivity of CuMnAs was observed after running a series of short (ms) electrical pulses. The experiment was done as pictured in Fig.1.1. In this setup, the directions of electrical pulses are perpendicular. Upon changing the direction of the electrical pulse, changes in sign of transverse resistivity were observed. These changes were in the orders of tenths of per cent. This result was attributed to AMR at that time. Parallel to measurements of changes in resistivity, XMLD-PEEM measurements showed the reconfiguration of magnetic domains depending on the direction of the current. The reconfiguration of magnetic domains corresponds to a 90° rotation. This confirmed that by running an electric current through the material, switching of magnetic domains is achieved.

In the experiment of [18], the antiferromagnet CuMnAs is switched by stag-

gered current-induced fields.[18] Term *staggered field* denotes a field that periodically changes its direction, usually with the spatial period of one lattice vector. This corresponds to the symmetry of the magnetic order in antiferromagnets. The method of staggered field relies on the asymmetry of an elementary cell in CuMnAs. Staggered fields arise under the condition that **MnA** and **MnB** in Fig.1.2 are inversion partners. The direction of the staggered field is opposite for each sublattice of the CuMnAs crystal.[18] Other methods of antiferromagnetic switching include the application of a strong magnetic field ($B = 2\,\mathrm{T}$).[14]

Switching of antiferromagnets moves the domain walls. This was detected by Ref.[19]. Domain wall separates magnetic domains, and its width in CuMnAs is $d \sim 10\,\mathrm{nm}$ to $100\,\mathrm{nm}$[19]. Domain wall motion in antiferromagnets has much faster dynamics than in ferromagnets.[19]

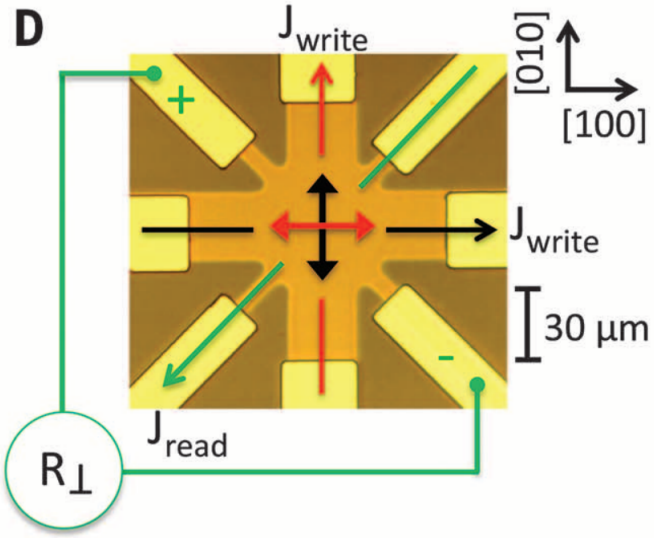

Figure 1.1: Scheme of writing pulses j and measurement of $R_\perp$. From Ref.[18]

1.1.1 Nanofragmentation of Domains

After the experiments showing the presence of Anisotropic Magnetoresistance in antiferromagnets[4, 18], new discoveries were made that report on much larger resistivity changes in the antiferromagnet CuMnAs[9], implying some completely different mechanisms are at play.

Bar-scheme

In 2021 up to 20% increase in resistivity was observed. During these experiments, a series of electric pulses was run through the material CuMnAs. The first version of the experiment was done using a simple bar scheme. The resistivity was measured along the direction of the applied pulse. The increase of resistivity was achieved by a $j \sim 10^7\,\mathrm{A\,cm^{-2}}$. After applying a second, slightly weaker pulse, resistivity decreases to approximately 50%. They estimate that the specimen reaches temperatures of $T = (200 \pm 50)\,^\circ\mathrm{C}$ during the pulsing, which means that Néel temperature is within the observational error of the measured value. It was

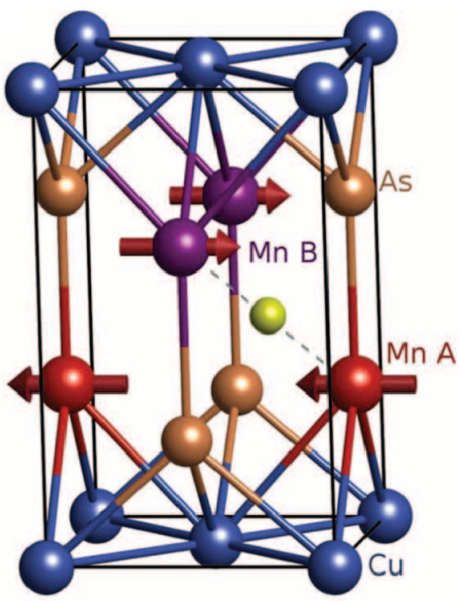

Figure 1.2: Crystal structure of **CuMnAs** and the **Mn** sublattices **A** and **B**. From Ref.[18]

also observed that the increase in resistivity due to the pulsing was temperature independent, which is surprising, as the resistivity of a material relates to temperature.[9]

Wheatstone bridge

The second version of the experiment is done as pictured in figure Fig.1.3. Wheatstone bridge is used to apply the current to different parts of the specimen. Furthermore, the temperature-dependent offset of resistivity is eliminated due to the $R_T = 0\,\Omega$ without the switching, R_T is calculated from the measured voltage in Fig.1.3. Pulses are applied either along the red-coloured or the black-coloured arms in Fig.1.3. The direction of pulses periodically changes. This method differs from the bar-scheme, where pulses are of different amplitude, but the direction stays the same.

The dependence of R_T on time is pictured in figure 1.4. The red-coloured curves represent the state of the system after applying the pulse along the red-coloured arms and analogously for the black curves. The change in sign for different directions of the pulses is the result of the symmetry of the Wheatstone bridge. The falling edge (dashed lines in figure Fig.1.4) depends on the delay between the pulses.

The Wheatstone bridge allows long-timescale measurements of resistivity. As shown in Fig.1.5, resistivity relaxes into lower values. However, relaxation times strongly depend on temperature. For instance, relaxation time for $T = 330\,\mathrm{K}$ is $\tau \sim 1\,\mathrm{s}$, for $T = 250\,\mathrm{K}$ relaxation time is much larger $\tau \sim 10^4\,\mathrm{s}$. The graph is fitted with Kohlrausch stretched exponentials $\exp[\frac{-\beta t}{\tau}]$. Where β is a fitted parameter. β also shows up in the theory of complex systems, and it depends on the dimension of the system $\beta = \frac{d}{d+2}$. The fitted value of β comes to $\beta = 0.6$. This result is in agreement with the theory of complex systems for $d = 3$. The fit contains two independent Kohlrausch stretched exponential components corresponding to two

different relaxation times.

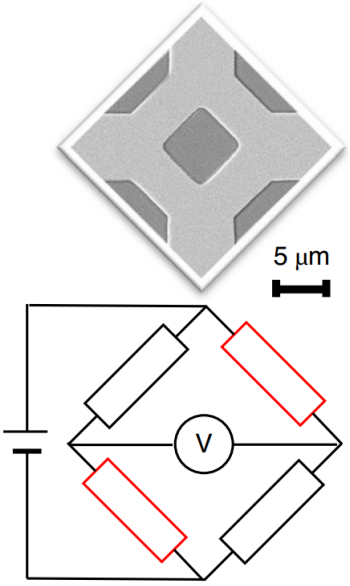

Figure 1.3: Scheme of a Wheatstone bridge From Ref.[9]

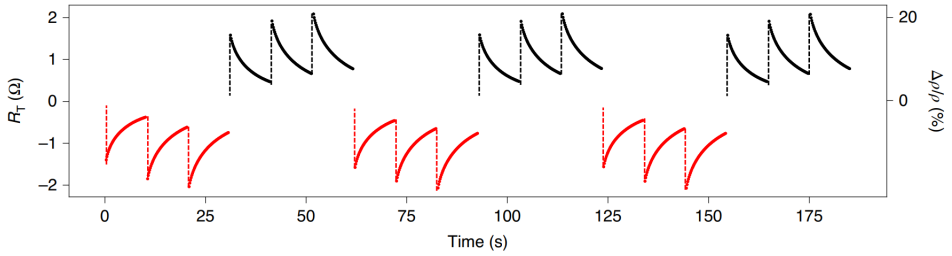

Figure 1.4: Dependence of $R_T(\Omega)$, which is measured across the sample by the voltmeter. It pictures the result of pulsing along a pair of red arms (Fig.1.3) with three pulses of the same amplitude and subsequently pulsing along the pair of black arms with three pulses of the same amplitude. From Ref.[9]

Optical switching

Similarly to electric current switching pictured in the scheme, Fig.1.3, switching can be achieved by optical pulses. This is done by alternatively applying optical pulses to the black/red arms of the Wheatstone bridge in Fig.1.3. The switching can be detected by measuring changes in resistivity or reflectivity. The experiments were done with 100 fs pulses. As with the electrical pulses, the energy delivered by one singular pulse is $u \sim 1\,\mathrm{kj\,cm^{-3}}$[9]. Optical pulse switching differs from electrical in its length - optical(fs) and electrical(ns).

XMLD-PEEM measurements

XMLD (X-ray magnetic linear dichroism) is a phenomenon where a different amount of linear-polarized light is absorbed, depending on whether it is polar-

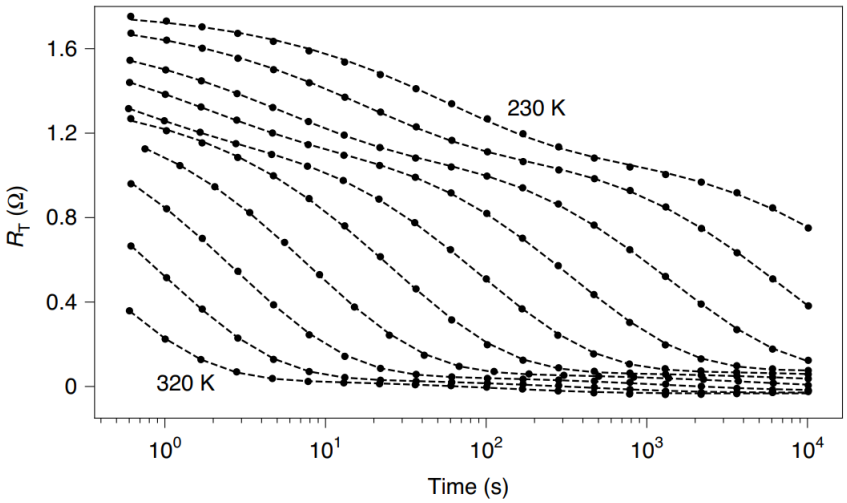

Figure 1.5: Dependence of resistivity R_T on time, fitted with Kohlrausch-stretched exponentials, temperature step between series of values is 10 K. From Ref.[9]

ized perpendicular or parallel to the magnetic orientation axis. The intensity of detected light depends on the direction of the electric field $\boldsymbol{E}$ of the polarized incident beam in relation to the antiferromagnetic orientation axis $\overleftrightarrow{A}$. The effect of XMLD allows only to observe the orientation of the antiferromagnetic axis $\overleftrightarrow{A}$. Therefore, only half of the antiferromagnetic domains are visible, and domains that differ by 180° rotation appear the same. Despite this limitation, it is a useful tool for analysing the microscopic structure of the antiferromagnetic domains. [15].

The detection in the CuMnAs experiments Ref.[9, 18, 19] was done via XMLD-PEEM (PEEM stands for photoemission electron microscopy). This is a special type of XMLD that is utilized to generate spatial resolution. Incident light is absorbed due to the photoelectric effect, and an electron is excited to a higher state. This creates an unoccupied state that subsequently decays, and secondary electrons are emitted and detected by an electron microscope. The PEEM method is used to generate spatial contrast in the image from the variations in the electron emission in the sample. Spatial resolution of PEEM is only 20 nm.[15]

Antiferromagnetic domains are pictured in Fig.1.6, the X-ray source was polarized along the E ∥ $[1\bar{1}0]$ crystallographic axis [9]. The results demonstrate a qualitative change in the structure of magnetic domains due to the electrical switching. In the measurement of a sample without pulsing, we see that size of the domains is $d \sim 10\,\mu$m. On the contrary, magnetic domains of the sample after pulsing are estimated to be of $d \sim 10$ nm in size. However, XMLD-PEEM does not reach such a small resolution. Measurements of the time development of the quench-switched sample show that it remembers the original pre-quenched state of the antiferromagnetic domains and relaxes towards its shape. [9]

NV-magnetometry results

NV (nitrogen vacancy) magnetometry is a microscopic method, that allows measuring the magnetic field with very high precision. It is used to reconstruct the

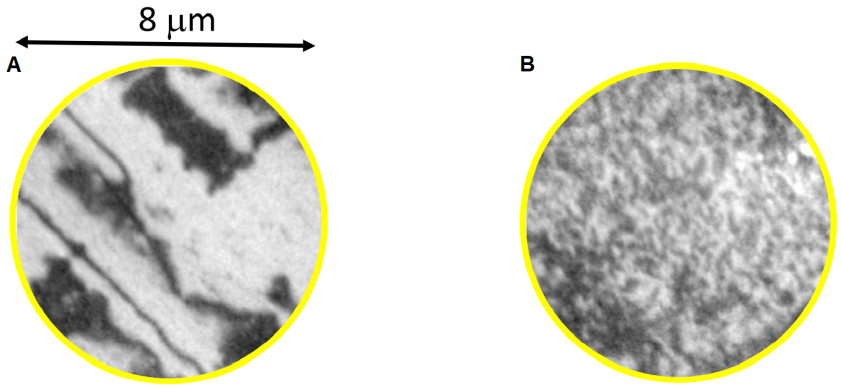

Figure 1.6: a) XMLD-PEEM image of magnetic structure CuMnAs on the substrate of GaP, b) image of the sample after applying a electric pulse $j \sim 10^7\,\mathrm{A\,cm^{-2}}$ for $t = 100\,\mathrm{ms}$ From Ref.[9]

alignment of magnetic moments for ferromagnets and antiferromagnets. As the probe, the nitrogen-vacancy centre, which is a point defect found in diamonds, is used. This defect consists of one carbon atom replaced by a nitrogen atom and the neighbouring carbon atom vacant. This method uses a scanning microscope with an NV centre positioned at its tip. The spin of the NV centre is influenced by the magnetic field located near the surface of the sample. This interaction shifts the electron spin resonance frequency. A shift in the resonance is then detected by a microwave field. The microwave field induces the NV centre to exhibit photoluminescence, which is then measured.[3]

One of the many applications of NV magnetometry is the observation of domain structure in an antiferromagnet. By analyzing the stray field detected by the NV centre, we can calculate the magnetic field at the position below the NV centre. To calculate the domain pattern, the antiferromagnet is modelled as two layers of opposite magnetic moment polarity. The magnetic moment cannot be unambiguously calculated, as the part of the magnetic field $\boldsymbol{m}$, for which $div\,\boldsymbol{m} = 0$, does not affect the magnetic stray field.[20]

NV magnetometry combined with XMLD-PEEM is used to measure the microscopic domain structure of the material CuMnAs. They are especially useful for measuring the domain structure changes after quench switching, as seen in Fig.1.7. The domain size after quench switching was estimated to be approximately $d \sim 10\,\mathrm{nm}$.[20]

[20] suggested that "The reduction of the stray field amplitude is caused by a decrease of the average domain size". The reduction of domain size is visible from Fig.1.7c) by comparing the structure with the white lines. The white lines also illustrate the memory of the pristine domain structure.

Interpretation of quench-switching experiments

It was observed that magnetic domains can be switched either electrically or optically. The observed rise in resistivity and the structural change of antiferromagnetic domains cannot be attributed to electric current. With both methods, the amount of transferred energy was of the same numeric order. This means that these changes are caused by heat. The domains are fragmented into smaller

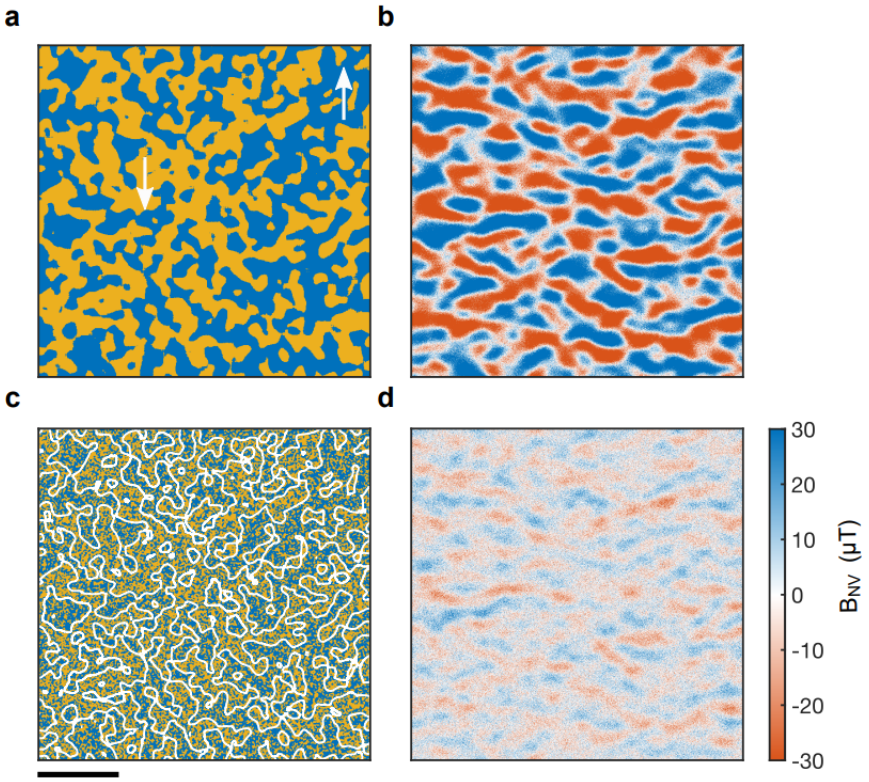

Figure 1.7: Figures in the left column represent the antiferromagnetic domains that are calculated from the simulated stray fields in the right column. The top row shows the pristine CuMnAs sample. The bottom row shows the quench switched (a series of $j \sim 10^7\,\mathrm{A\,cm^{-2}}$ pulses with time duration of $t = 100\,\mu\mathrm{s}$) figures of the CuMnAs sample. The white arrows are Neél vectors. Size bar is 400 nm. The white borders in c) are the domain walls taken from figure a) and overlapped into c) for comparison. Scale bar in bottom right pictures the magnitude of the magnetic stray field B_{NV} assigned to colour spectrum From Ref.[20]

domains. The quench switching does not rotate the magnetic moments. This is different from the findings of Ref.[19], which detected a 90° rotation of magnetic moments.

Changes in the resistivity of the sample were observed after quench switching. At the same time, XMLD-PEEM and NV magnetometry methods show nano-fragmentation of antiferromagnetic domains after the pulsing. The exact reasons for the nano-fragmentation and the resistivity increase remain unclear.

1.2 Landau-Lifshitz-Gilbert equation

1.2.1 Undamped system

We start this section by considering a simple system without damping. Similarly to classical mechanics, torque $\boldsymbol{T}$ acts upon the spin $\boldsymbol{S}$ of a electron as described by the following equation:

$$\boldsymbol{T} = \frac{d\boldsymbol{S}}{dt} \tag{1.2}$$

Moreover, the torque $\boldsymbol{T}$ on a magnetic moment $\boldsymbol{M}$ is:

$$\boldsymbol{T} = \boldsymbol{M} \times \boldsymbol{B} \tag{1.3}$$

where $\boldsymbol{B}$ is an effective field. Magnetic moment $\boldsymbol{M}$ of an electron is related to the electrons spin through:

$$\boldsymbol{M} = \gamma \boldsymbol{S} \tag{1.4}$$

where γ is the electron gyromagnetic ratio. Joining the equations Eq. (1.2), Eq. (1.3), Eq. (1.4), we arrive at the undamped equation for magnetic moments:

$$\frac{d\boldsymbol{M}}{dt} = \gamma \boldsymbol{M} \times \boldsymbol{B} \tag{1.5}$$

$\boldsymbol{B}$ can be calculated as:

$$\boldsymbol{B} = -\frac{\partial U(\boldsymbol{M})}{\partial \boldsymbol{M}} \tag{1.6}$$

where ∂U is the work done by rotating the magnetic moment. The vector variables could be assigned to discrete points in space. In our case, it would be the atoms of the lattice.

1.2.2 Damped system

In a system with non-zero damping, the dynamics of atomic magnetic moments are governed by the Landau-Lifshitz-Gilbert equation. This is a system of coupled non-linear differential equations. An analytic solution exists only in a few very simple systems. In our research, simulations are done with such large systems that an analytic solution is unfeasible and a numerical approach must be used.

The master equation of atomistic spin dynamics is the Landau-Lifshitz-Gilbert equation:

$$\frac{\partial \boldsymbol{M}_i}{\partial t} = -\gamma \boldsymbol{M}_i \times \boldsymbol{B}_i + \frac{\alpha}{M_i} \boldsymbol{M}_i \times \frac{\partial \boldsymbol{M}_i}{\partial t} \tag{1.7}$$

[5]

where α is the damping parameter and the index i denotes the i-th atom. The first term in equation Eq. (1.7) describes the precessional motion, which was described in subchapter 1.2.1, and the second describes the damping. The second term is proportional to $\boldsymbol{M}_i$. That is similar to the mechanics of continuum, where the dissipative force is proportional to the velocity and of the opposite direction.

Let us compare equation Eq. (1.7) to the equation presented by Landau and Lifshitz [10], which is the equation used in the following simulations. The reason for the use of these equations is that they are easier to calculate numerically compared to the Eq. (1.7), as Eq. (1.7) is written in the implicit form (with

the magnetization time derivative on both sides of the equation). The Landau-Lifshitz equation is written in the following form:

$$\frac{\partial \boldsymbol{M}_i}{\partial t} = -\gamma \boldsymbol{M}_i \times \boldsymbol{B}_i - \frac{\lambda}{M_i^2} \boldsymbol{M}_i \times (\boldsymbol{M}_i \times \boldsymbol{B}_i) \tag{1.8}$$

λ is a phenomenological constant. It relates to α:

$$\lambda = \alpha \gamma M \tag{1.9}$$

1.2.3 Difference between Landau - Lifshitz and Landau - Lifshitz - Gilbert equation

How do the Landau-Lifshitz-Gilbert and Landau-Lifshitz equations compare? Are they equivalent? For the following derivation, it will be helpful to prove this statement:

$$\boldsymbol{M} \cdot \frac{\partial \boldsymbol{M}}{\partial t} = 0 \tag{1.10}$$

We multiply Eq. (1.7) by $\boldsymbol{M}$ from the left:

$$\boldsymbol{M} \cdot \frac{\partial \boldsymbol{M}}{\partial t} = -\gamma \boldsymbol{M} \cdot (\boldsymbol{M} \times \boldsymbol{B}) + \frac{\alpha}{M} \boldsymbol{M} \cdot \left(\boldsymbol{M} \times \frac{\partial \boldsymbol{M}}{\partial t} \right)$$
$$\boldsymbol{M} \cdot \frac{\partial \boldsymbol{M}}{\partial t} = \gamma \boldsymbol{B} \cdot (\boldsymbol{M} \times \boldsymbol{M}) + \frac{\alpha}{M} \frac{\partial \boldsymbol{M}}{\partial t} \cdot (\boldsymbol{M} \times \boldsymbol{M}) = 0$$

Since $\boldsymbol{M} \parallel \boldsymbol{M}$, both terms in the parentheses are zero, and the statement is thus proved. Now we amend the Landau-Lifshitz-Gilbert equation by multiplying from the left.

$$\boldsymbol{M} \times \frac{\partial \boldsymbol{M}}{\partial t} = -\gamma \boldsymbol{M} \times (\boldsymbol{M} \times \boldsymbol{B}) + \frac{\alpha}{M} \boldsymbol{M} \times \left(\boldsymbol{M} \times \frac{\partial \boldsymbol{M}}{\partial t} \right)$$
$$\boldsymbol{M} \times \frac{\partial \boldsymbol{M}}{\partial t} = -\gamma \boldsymbol{M} \times (\boldsymbol{M} \times \boldsymbol{B}) - \alpha M \frac{\partial \boldsymbol{M}}{\partial t}$$

Where we used the equation Eq. (1.10) along with the identity $\boldsymbol{A} \times (\boldsymbol{B} \times \boldsymbol{C}) = (\boldsymbol{A} \cdot \boldsymbol{C})\boldsymbol{B} - (\boldsymbol{A} \cdot \boldsymbol{B})\boldsymbol{C}$. Now we substitute equation above into the LLG equation Eq. (1.7).

$$\frac{\partial \boldsymbol{M}}{\partial t} = -\gamma \boldsymbol{M} \times \boldsymbol{B} - \frac{\alpha\gamma}{M} \boldsymbol{M} \times (\boldsymbol{M} \times \boldsymbol{B}) - \alpha^2 \frac{\partial \boldsymbol{M}}{\partial t} \tag{1.11}$$

By rearranging the equation, we obtain:

$$\frac{\partial \boldsymbol{M}}{\partial t} = -\gamma_L \boldsymbol{M} \times \boldsymbol{B} - \frac{\gamma_L \alpha}{M} \boldsymbol{M} \times (\boldsymbol{M} \times \boldsymbol{B}) \tag{1.12}$$

where we introduced new term $\gamma_L = \frac{\gamma}{1+\alpha^2}$. From this equation we see that Landau-Lifshtitz equation Eq. (1.8) differs from Landau-Lifshitz-Gilbert Eq. (1.7) in that the γ_L depends on α. For small enough α, equations are equal.

1.2.4 Magnetic energy

Magnetic energy U_j of a j-th spin is, in our case, determined by the sum of two energy components:

$$U_j = U_{ex}(\boldsymbol{M}_i) + U_a(\boldsymbol{M}_i) \tag{1.13}$$

where $U_{ex}(\boldsymbol{M}_i)$ is the exchange energy and $U_a(\boldsymbol{M}_i)$ is the anisotropy energy. These will be important for this work. $\boldsymbol{M}_i$ denotes the set of all magnetic moments that contribute to the magnetic energy.

Exchange energy corresponds to the interaction between neighbouring atomic moments. This interaction is responsible for the magnetic ordering of spins. It depends on their relative direction - or the angle between the vectors. Hence, we perform a dot product between the magnetic moments in the exchange energy formula. It takes the form of:

$$U_{ex} = -\sum_{\langle ij \rangle}^{N} J_{ij} \left(\frac{1}{M_i M_j} \boldsymbol{M}_i \cdot \boldsymbol{M_j} \right) \tag{1.14}$$

Here, J_{ij} is the exchange constant, $\langle$ij$\rangle$ means that the sum goes over the unique pairs of ij, $\boldsymbol{M}_i$ is the magnetic moment of the electron at position i of the lattice, M_i is the norm of magnetic moment $\boldsymbol{M_i}$. If the exchange constant $J_{ij} < 0$, spins prefer antiparallel alignment, so the material is antiferromagnetic. For the opposite case $J_{ij} > 0$, the spins want to align parallel to each other. Thus the material is ferromagnetic.

Magnetocrystalline uniaxial anisotropy energy of the lowest order for tetragonal crystals is:

$$U_a = \sum_{i}^{N} \left(\frac{K}{M_i^2} \boldsymbol{K} \cdot \boldsymbol{M_i} \right)^2 \tag{1.15}$$

where N is the number of atoms, K is the anisotropy strength, $\boldsymbol{K}$ is the anisotropy axis, and n_i is the spin of an electron at lattice point i. The lowest order in-plane anisotropy in tetragonal crystals can be written as:

$$U_{bi-a} = \sum_{i}^{N} \frac{K_{bi}}{M_i^4} (M_{ix}^4 + M_{iy}^4) \tag{1.16}$$

The anisotropy defined in the equation above is called biaxial anisotropy. The K_{bi} is the biaxial anisotropy strength, M_{ix} and M_{iy} are the x, y components of the magnetic moments at site i, respectively.

2. Simulations of atomistic spin dynamics

2.1 The spirit Library

The spirit framework is a tool for computing the atomistic spin dynamics for a large number of spins. This is very convenient for the field of spintronics, which requires such large scales.

In our simulations, the method of Landau-Lifshitz differential equations was used. The exact equations that the algorithm solves are the same as Eq. (1.12). However, instead of $\boldsymbol{B}$, an amended field is used.[12]

$$\boldsymbol{B}_i^{\text{eff}} = \boldsymbol{B}_i + \boldsymbol{B}_i^{\text{th}} \tag{2.1}$$

, where $\boldsymbol{B}_i = \frac{\partial U}{\partial \boldsymbol{M}_i}$ is the term caused by the energy derivative, and $\boldsymbol{B}_i^{\text{eff}}$ is the stochastic thermal term, which is defined as:

$$\boldsymbol{B}_i^{\text{eff}} = \sqrt{2D_i}\boldsymbol{\eta}_i(t) = \sqrt{2\alpha k_B T \frac{\mu_i}{\gamma}}\boldsymbol{\eta}_i(t) \tag{2.2}$$

Here, D_i is the diffusion constant, α is the damping parameter, μ_i is the i-th magnetic moment, γ is the gyromagnetic ratio, and T is temperature. The term under the square root on the right side comes from the fluctuation-dissipation theorem. It states that if the system dissipates energy, then thermal fluctuations will arise.[2] A classical example of the fluctuation-dissipation theorem would be the drag force and Brownian motion. $\boldsymbol{\eta}_i$ is white noise, which must satisfy these conditions:

$$\langle \boldsymbol{B}_{i\alpha} \rangle = 0 \tag{2.3}$$

$$\langle \boldsymbol{B}_{i\alpha}^{th}(t)\boldsymbol{B}_{j\beta}^{th}(0)\rangle = 2D_i\delta_{ij}\delta_{\alpha\beta}\delta(t) \tag{2.4}$$

To simulate the sudden electrical or optical pulse that was used in the experiment of [9], we assume that the pulse introduces a lot of heat into the system. The heat raises the temperature above the Néel temperature, which is the point where a material loses its magnetic ordering. After the pulse ends, the source of the heat is cut off, the sample cools below Néel temperature, and the spins will form small antiferromagnetic domains. This disordered state is taken as a starting point for the ensuing simulations. The objective is to simulate the formation of antiferromagnetic domains at various temperatures.

The spirit library has many options for user interfaces. GUI can be used. However, the command line user interface offers much more functions. Spirit library implemented in python was used to perform the simulations in this work.

2.2 Plotting of the atomic spins

Ploting of the final Néel vectors is done via a python script called plot_L.py. It plots the spherical angles θ and φ, used to describe the position in 3D spherical coordinates. These angles are defined as:

$$\theta = \arccos\left(\frac{L_z}{\sqrt{L_x^2 + L_y^2 + L_z^2}}\right) \tag{2.5}$$

$$\varphi = \mathrm{sgn}(L_y)\arccos\left(\frac{L_x}{\sqrt{L_x^2 + L_y^2}}\right) \tag{2.6}$$

To properly graph those two angles, we need two subplots. The left plot graphs the angle φ, and the right plot graphs the angle θ e.g. Fig.2.3. For graphing of the angles, a colour scheme is used. The colour scheme for φ is pictured in Fig.2.1 and for θ in Fig.2.2. Vectors in the left subplot are identical to the vectors on the right. They plot the projection of the Néel vector to the x-y plane. It would be impractical to graph all Néel vectors, especially in large systems. So an average vector is calculated from the neighbouring cells. For example, in a system of $300 \times 300 \times 1$ basis cells, we only plot $60 \times 60 \times 1$ vectors. The average vector is then calculated from 25 neighbouring vectors, a square with a side of five spins. Averaged Néel vector array will be referred to as the grid. In our example, grid $= [60, 60, 1]$.

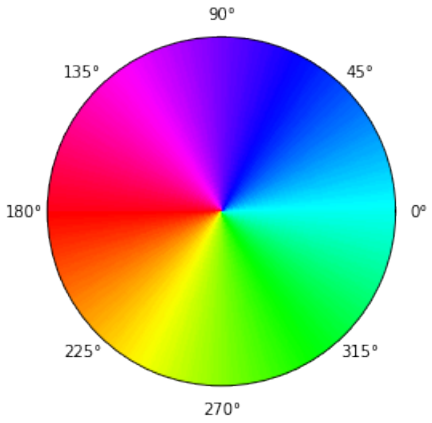

Figure 2.1: The interval of possible values of the angle $\varphi \in \langle 0,\, 2\pi)$ is represented by a color spectrum.

2.3 Simulations with different time steps

To solve the LL equation Eq. (1.12) we start from some initial state, which gives the magnetic moments at time $t = 0$. To solve the LL equation Eq. (1.12), we start from some initial state, which gives the magnetic moments at time $t = 0$. In the simulations, the SIB (Semi-implicit midpoint) solver was used. The method consists of approximating the derivative in the point halfway between t and $t+\Delta t$ by the slope of $\boldsymbol{M}_i(t + \Delta t)$ - $\boldsymbol{M}_i(t)$. However, the derivative is dependent on the configuration of magnetic moment in time $t + \Delta t$. However, the derivative is dependent on the configuration of magnetic moment in time $t+\Delta t$. The equations have this form:

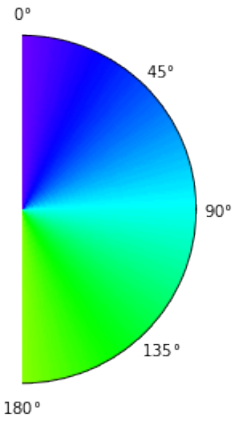

Figure 2.2: The interval of possible values of the angle $\theta \in \langle 0, \pi)$ is represented by a color spectrum.

$$\begin{aligned} \boldsymbol{M}_i(t+\Delta t) =& \boldsymbol{M}_i(t) + \Delta t \frac{\boldsymbol{M}_i(t) + \boldsymbol{M}_i(t+\Delta t)}{2} \\ & \times \boldsymbol{A}_i \left(t + \frac{\Delta t}{2}, \left\{ \frac{\boldsymbol{M}_j(t) + \boldsymbol{M}_j(t+\Delta t)}{2} \right\} \right) \end{aligned} \tag{2.7}$$

The index i denotes the i-th magnetic moment, $\boldsymbol{A}_i$ is defined as follows:

$$\boldsymbol{A}_i = -\gamma_L (\boldsymbol{B}_{\text{eff}} + \frac{\alpha}{M} (\boldsymbol{M}_i \times \boldsymbol{B}_{\text{eff}})) \tag{2.8}$$

This definition is derived from the LL Eq. (1.12). The term in the curly brackets corresponds to the set of all magnetic moments in the system. The problem is this equation is written in the implicit form since $\boldsymbol{M}_j(t+\Delta t)$ stands on both sides of the equation. This is sorted out by approximating $\boldsymbol{M}_j(t+\Delta t)$ by a predictor moment $\boldsymbol{M}_j^p$, which is defined again by the implicit middle point structure:

$$\boldsymbol{M}_i^p(t+\Delta t) = \boldsymbol{M}_i(t) + \Delta t \frac{\boldsymbol{M}_i(t) + \boldsymbol{M}_i^p(t+\Delta t)}{2} \boldsymbol{A}_i \left(t, \{\boldsymbol{M}_j(t)\}\right) \tag{2.9}$$

To avoid the implicit term in $\boldsymbol{A}_i$, the $\boldsymbol{A}_i$ is approximated in the relation for the predictor $\boldsymbol{M}_j^p$. After the $\boldsymbol{M}_j^p$ is obtained, the equation is implicit only in terms outside of $\boldsymbol{A}_i$ and can then be solved.[11]

The SIB method is very sensitive to the value of the time step Δt. Therefore, it is needed to test how it influences the time development of the magnetic moments. If the time step Δt was too big, it could be in contradiction with the assumption of the tangent $\frac{\partial \boldsymbol{M}_i}{\partial t}(t + \frac{\Delta t}{2})$ being parallel to the line segment between the two time points. In practice, this discrepancy could have an impact on larger time scales. One could then wind up with qualitatively different results from those with a smaller time step. Theoretically, the smaller the time step, the more precise simulation is achieved.

However, after the time step gets smaller than a certain value, it becomes quite redundant to decrease the time step further. The drawback of superfluously small time step is that it requires more iterations to simulate the time development of the system. In the simulation, the system was already quite large. It consisted

of millions of magnetic moments and was simulated on the scales of hundreds of picoseconds. This meant that in order for the simulations to run with enough time efficiency, it was needed to maximize the value of the time step Δt while maintaining reasonable correspondence with the simulations that use smaller time steps. This was done in simulations shown in Fig.2.3.

As mentioned before, to simulate the heating of the sample, as was done in experiment [9], the spins in the initial state are aligned randomly. Therefore the exchange interaction is significant in the first few picoseconds. This means one needs to carefully choose the time step. The decision was made to run the simulation in the first 2 ps with the time step $\Delta t = 0.1$ fs, which is much smaller than the other time steps that were tested. The simulations of time steps $\Delta t_1 = 0.5$ fs and $\Delta t_2 = 1$ fs were then done with the initial state of spins, which were taken as the final spins of the simulation with $\Delta t = 0.1$ fs, which lasted for $t = 2$ ps. In other words, when the dynamics of the system are fast, we used a very small time step, and after that, we tested two bigger time steps. This ensures that our calculations are both accurate and efficient.

In Fig.2.3, two simulations with different time-steps Δt are compared, both images show the simulations in time $t = 30$ ps. Although from afar, the two images in Fig.2.3 look identical, zoomed in and overlapped, it could be seen that they do differ in certain areas. These areas are located in a domain wall, precisely in the area where spins rotate around a point. However, these differences are very small. Therefore, it was concluded that the time step of $\Delta t = 1$ fs was satisfactory enough since the simulations do not significantly differ from those done with the $\Delta t = 0.5$ fs. In the end, the decision was made to run the whole simulation with the time-step of $\Delta t = 1$ fs.

2.4 Simulations with different anisotropy constant

It is important to determine the values of parameters, such as in-plane anisotropy constant and damping parameter, before proceeding with more complex simulations. Theoretical calculations report on the very small difference between biaxial anisotropy energies for the direction [100] and [110]. The difference was less than 1 μeV. The difference between the energies in [100] and [001] was significantly larger, about 127 μeV. This result stems from relativistic ab-initio calculations.[17]

Both in-plane ($\hat{\boldsymbol{x}}$ and $\hat{\boldsymbol{y}}$ direction) uniaxial and biaxial anisotropy were observed in the crystal CuMnAs. In principle, tetragonal lattice allows biaxial anisotropy only to exist. However, in thin layers, the symmetry can be broken. This could lead to uniaxial in-plane anisotropy. There is always out-of-plane ($\hat{\boldsymbol{z}}$ direction) present. The kind of in-plane anisotropy that arises depends on the method of growth of the crystal that was used. In the following simulations, uniaxial in-plane anisotropy in the direction [100] was tested. The in-plane biaxial anisotropy was ignored for simplicity.

Fig.2.4 suggests that, with a growing in-plane anisotropy constant, the domain walls become larger. In the bottom row of Fig.2.4, we see that almost the whole system is covered by a single domain. In the subplot in the top row, left column

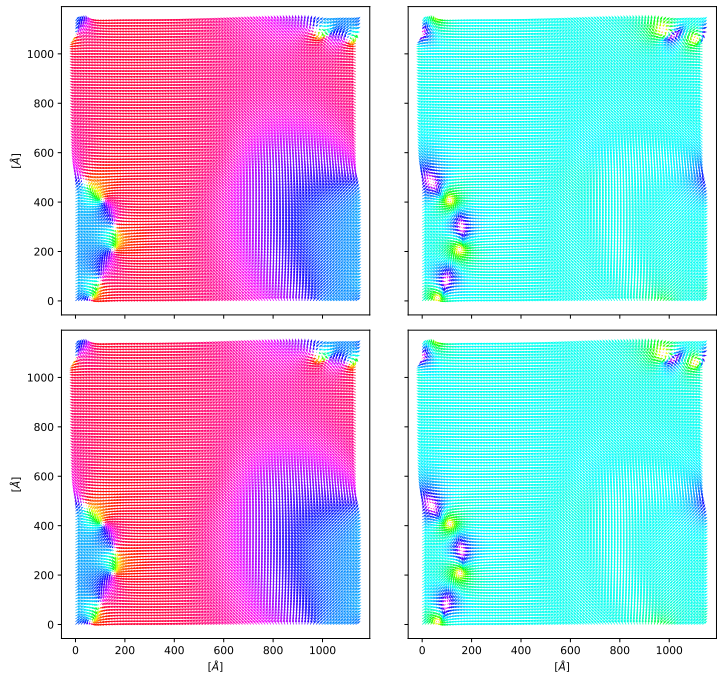

Figure 2.3: Comparison of two simulations. Simulation in the top row was done with the time step $\Delta t = 1\,\text{fs}$. Image is taken after $N = 30000$ iterations. Simulation in the bottom row was done with the time step $\Delta t = 0.5\,\text{fs}$. The image was taken after $N = 60000$ iterations. Both plots represent the simulation in time $t = 30\,\text{ps}$ Plotted with grid $= [100, 100, 1]$

of Fig.2.4, the giant domain that is pictured by the green-coloured vectors could be seen. Other domains are not clearly visible. However, a second domain is positioned in the top left corner. Due to large domain walls, the transition between one domain and the other could not be unambiguously recognised. Parts of the second domain wall penetrate into the top right and the bottom left corner. This is due to the periodic boundary conditions.

The values of $K = 0.1$ and $K = 0.05$ are of the same order as the out-of-plane uniaxial anisotropy constant, and we know that the out-of-plane anisotropy is stronger. Therefore it is reasonable to exclude those values from further simulations. There are no experimental values of the uniaxial or biaxial anisotropy. From calculations, it is known that the value of biaxial anisotropy is $K = 0.001$ or less. However, there are no calculations for the uniaxial anisotropy constant available. It is reasonable to estimate that the value of uniaxial in-plane anisotropy will be smaller than the value of the out-of-plane anisotropy. The exchange interaction should also be stronger than the in-plane anisotropy interaction. However, if we set the value of the in-plane anisotropy constant to be very small, it could negatively influence the speed of the numerical calculations. For further simulations, the uniaxial anisotropy constant was set to a value of $K = 0.01$.

2.5 Simulations with different damping parameters

Damping dissipates energy and brings the system to its equilibrium. If the damping was zero, the system would precess around the point of equilibrium. The damping parameter influences the dynamics of magnetic domains formation. If an external field is applied in the $\hat{\boldsymbol{z}}$ direction, the magnetic moment is aligned in a direction that is not parallel to the external field. The magnetic moment will behave as prescribed by the LLG Eq. (1.7). It will precess around the $\hat{\boldsymbol{z}}$ axis. The damping parameter does not influence the dynamics of precession. However, the damping drives the magnetic moment to the equilibrium direction, which is the magnetic field direction. This torque is perpendicular to the precessional torque. It is caused by the damping term. The speed of relaxation into the direction is proportional to the damping parameter. This is a very simple example. In our calculations of millions of spins, it may behave differently.

In Fig.2.5, two simulations with different damping parameters are compared. The damping parameter of the first simulation is two times smaller than that of the second one. Moreover, the first simulation is captured in the time of $t = 40\,\mathrm{ps}$, which is two times smaller than the time in which the second simulation is captured $t = 80\,\mathrm{ps}$. This would suggest that the relaxation speed is inversely proportional to the damping parameter. This is counter-intuitive. One would expect, based on the simple example above, that with growing damping parameter, the domain dynamics would get faster.

In Fig.2.6, we see a comparison of three simulations with different damping parameters α captured at the same time $t = 90\,\mathrm{ps}$. Again, we see that for smaller values of α, the domain size is greater. The exact reasons for this behaviour are unclear.

In the bottom row of Fig.2.6, the value $\alpha = 0.3$ of the damping parameter was used. The image differs from the others quite significantly. The domains are much smaller. For further simulations, the damping parameter was set to $\alpha = 0.1$.

2.6 Algorithm for calculating the average size of the antiferromagnetic domains

While the graphing of antiferromagnetic Néel vectors gives information about the contours and shapes of antiferromagnetic domains, it might be hard to extract any quantitative values from these plots. The quantity of the utmost interest is the mean size of the antiferromagnetic domains. As mentioned earlier in experiments done by [9], the changes in the size of antiferromagnetic domains were observed on macroscopic timescales. For this reason, we create an algorithm that approximately calculates the mean value of magnetic domains in a given time point.

As input, the algorithm takes a 3D list of Néel vectors, e.g. in a system with grid $= [60, 60, 1]$, we would have $n = 60 \times 60$ Néel vectors. The program randomly selects one Néel vector and compares it with its neighbouring vectors. Neighbouring vectors are those that are one lattice vector away, either horizontally

or vertically. Note that diagonal neighbours are not considered. The comparison is done with the following condition:

$$\epsilon \geq \|\boldsymbol{m_N} - \boldsymbol{m_0}\| \tag{2.10}$$

where $\boldsymbol{m_0}$ is the original random Néel vector, $\boldsymbol{m_N}$ is the neighbouring Néel vector, ϵ is a parameter that, in essence, determines how similar the vector must be in order to be considered as part of the domain that is defined by the original vector. If the condition Eq. (2.10) is satisfied, the neighbouring vector is considered to be part of the same domain as the original randomly selected vector. The same process is then repeated for the neighbouring vectors until there are not any more neighbours left to visit. Then the process is finished, and a list of coordinates of all vectors that belong to the domain is returned. This is repeated for the remaining spins.

2.6.1 Plotting of the categorized domains

In Fig.2.7, categorized domains for different values of ϵ are pictured. Coordinates that belong to the same domain are pictured with the same original Néel vector that was used in the condition Eq. (2.10).

Examining the plots for different values of ϵ, it could be seen that with growing ϵ, the greatest domains get bigger in size while the smaller ones shrink. Albeit, this effect is small, considering that the condition Eq. (2.10) lies at the core of the domain categorization algorithm.

One can compare the effectiveness of our algorithm by comparing Fig.2.7 with Fig.2.8, which plots all Néel vectors using the plot_L.py script. The conclusion of this comparison is positive, the algorithm rightly categorizes one or two big domains, and the domain wall is categorized as multiple smaller domains. The smaller domains can be ignored by introducing another condition that discards domains smaller than some cutoff number A_{min}. The value of the cutoff A_{min} will be discussed later. It is obvious that the algorithm is not capable of recognizing domain walls. Especially in the case of continuous, broad domain walls, it is not clear where one domain ends, and another begins.

How does the grid parameter affect the size of the domains? The grid should be chosen based on the size of the system. The grid should be proportional to the size of the system. This ensures that the number of Néel vectors in a given grid cell is constant.

2.6.2 Dealing with domain walls

As seen in Fig.2.9 majority of categorized domains are small. Around 250 domains occupy the first bin in our histogram. Then the next bin is occupied by one domain, and the last bin with the area of $A = 0.08\,\mu\text{m}^2$ is occupied by one domain. Groups of vectors within the first bin are not domains. They are rather parts of the domain wall, as could be seen in Fig.2.7. Therefore, it is reasonable to discard those domains that are smaller than some cutoff number A_{min}. A_{min} is the number of grid cells or Néel vectors. After analysing the histogram, A_{min} value was set to $A_{\text{min}} = 100$ which is equivalent to the area of $A = 4 \cdot 10^{-3}\,\mu\text{m}^2$.

The average size of domains is calculated the same way as the histogram of domain size in Fig.2.9. However, due to the random choice of the original Néel vectors of the domain in the algorithm, the process is somewhat random. That means that when the algorithm analyses the same configuration of Néel vectors, it returns domains that can slightly differ in shape and overall size. To mitigate this randomness, the algorithm in Fig.2.12 is called 15 times, and the average surface area of the domains shown in the figure is the average of those 15 iterations.

2.7 Time-development of the average domain size

In Fig.2.10, Fig.2.11 the time development of antiferromagnetic domains starting from the disordered state for two different sizes of the system is plotted. In Fig.2.10, the antiferromagnetic domains are quite large. After 50 ps, the system is covered by one large domain. The average domain size is visible in Fig.2.12

It is visible in Fig.2.12 that around time $t = 80\,\text{ps}$ the size of domains reaches a maximum, only to decrease in $t = 90\,\text{ps}$ to a value comparable to $t = 70\,\text{ps}$. This is an anomaly which is caused by the randomness of the initial spin field state and of the complexity of the spin dynamics. For instance, we do not observe such a peak in Fig.2.13, which was done with the same parameters, except the size of the system was bigger. In both figures, Fig.2.12 and Fig.2.13, growth of the average size of the domains is observed.

Notably, the size of the domains is much greater than the experimental values even in $t = 10\,\text{ps}$. The width of the domains is in orders of $d \simeq 100\,\text{nm}$. The experiments of [9] showed the domains to remain in the state of nano-fragmentation with widths $d \simeq 10\,\text{nm}$ for much longer periods of time. This suggests that what we see in the simulations does not correspond to the experiments.

2.8 Simulations with non-zero temperature

The experiments of [9] that were mentioned in the introduction were done in a room temperature setting. So far, we have done all simulations with the temperature of $T = 0\,\text{K}$. However, it is difficult to plot the results of the simulations. This is because, in a non-zero temperature system, magnetic moments oscillate around their equilibrium directions. Hence, the magnetic domains are not clearly visible, and it is hard to draw conclusions from such graphs. There are two solutions to this issue. The first would be to record the oscillations of these moments for some short time and then average those magnetic moments. The second solution is to take the magnetic moments at a particular time point t and run a new simulation with zero temperature for a very short time δt. The time duration of the simulation should be chosen such that the magnetic moments have enough time to move into their equilibrium. However, δt should be small enough that the system does not undergo further development during this time. Delta was set to a value of $\delta t = 2\,\text{ps}$. The second approach to the problem was chosen, as it was easier to implement than the first one.

In figure Fig.2.14, it can be seen that simulation with $T = 0\,\text{K}$ has one big domain. The simulation with $T = 300\,\text{K}$ has more domains (per our estimate three).

Unsurprisingly, these simulations developed differently. The thermal fluctuations have a non-trivial effect on the dynamics of the system.

In Fig.2.15 the time development of the spins in $T = 300\,\mathrm{K}$ is plotted. The antiferromagnetic domains are smaller compared to those with zero temperature. In Fig.2.16 time development of the average size of magnetic domains is pictured. Results of these preliminary room-temperature simulations suggest that antiferromagnetic domains are smaller than those in zero-temperature simulations.

2.9 Skyrmions and Half-skyrmions

We have already discussed domains and domain walls. However, there are many options for how the spins could re-orient when transitioning from one domain wall to another. In other words, domain walls could have different structures. One type of this structure is a Bloch-type wall, where spins rotate around an axis that is normal to the domain wall. Therefore the rotation of the spins is out-of-plane (the plane in which the domains lie). The second kind of structure is the Néel-type wall. The spins rotate around an axis that is perpendicular to the normal of the domain wall.[1] In our case, domain walls are of the Néel type.

Stable quasi-particles called merons can be found in domain walls. Merons are also sometimes called half-skyrmions. They are a version of their more famous relative skyrmion. Skyrmions and merons are topologically non-trivial objects. They possess a physical property called topological charge. These quasi-particles could potentially be used to store information.

Half-skyrmions were reported in material CuMnAs in an experiment by [1]. It was discovered that half-skyrmions could be created and moved by an electric current. In our simulations with the spirit library, half-skyrmions were also observed. See Fig.2.17. Those half-skyrmions played a role in the dynamics of domain formation. Half-skyrmions introduce inhomogeneity of spin orientation. Thus, the fewer half-skyrmions in the system, the more homogenous the system will be, and the more domains are present. Half-skyrmions often annihilate with a half-skyrmion of opposite chirality. There are multiple types of half-skyrmions. They differ in the way the spins rotate around a specific point. In Fig.2.17, the rotation of spins in the x-y plane is visible, and the z component of the spins is shown in the right subplot. In the centre of the half-skyrmion, the Néel vector points in the $\hat{\boldsymbol{z}}$ direction.

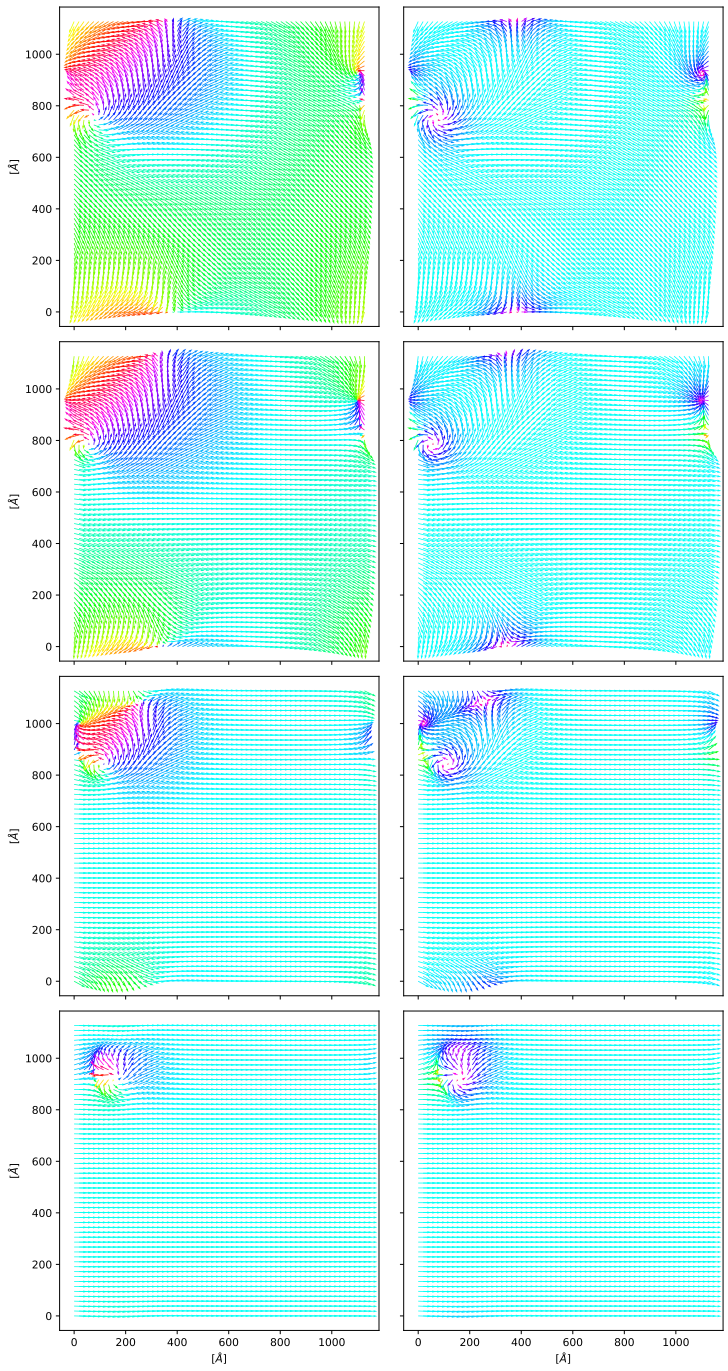

Figure 2.4: Simulations with different anisotropy constants in the direction [100]. Simulations are ordered in ascending order of the anisotropy constants. The first row from the top is $K = 0.001$. Second row $K = 0.01$. Third row $K = 0.05$. Fourth row $K = 0.1$. The size of the system is $300 \times 300 \times 1$ of basis cells. Plotted with grid $= [60, 60, 1]$. All simulations are captured in time $t = 100\,\text{ps}$. Damping parameter is $\alpha = 0.3$

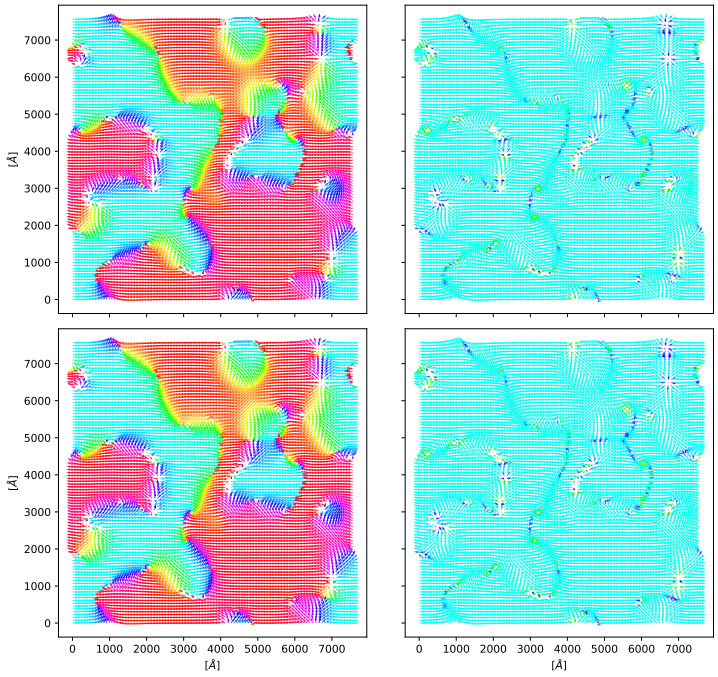

Figure 2.5: Comparison of two simulations. A simulation with damping parameter $\alpha = 0.05$ in time $t = 40\,\text{ps}$ is pictured in the top row. The bottom row corresponds to $\alpha = 0.1$ in time $t = 80\,\text{ps}$. All figures were done in time $t = 90\,\text{ps}$. The size of the system is $2000 \times 2000 \times 1$ of basis cells. Plotted with grid $= [100, 100, 1]$

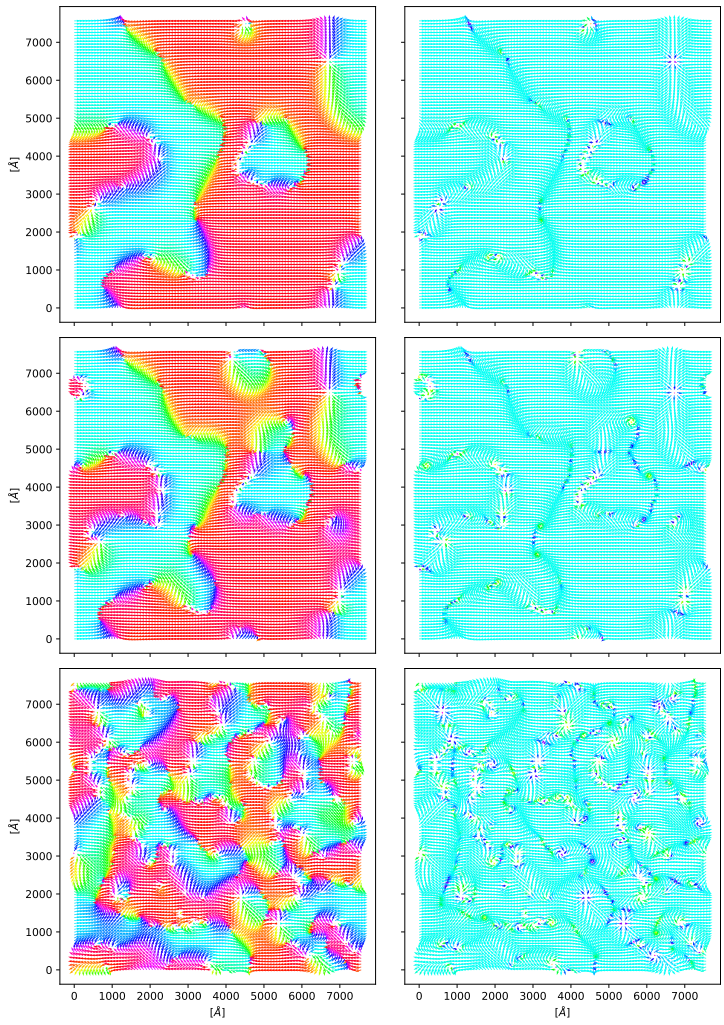

Figure 2.6: Simulations with different damping parameters. Graphs in the top row represent damping $\alpha = 0.05$. $\alpha = 0.1$ for middle row and $\alpha = 0.3$ for bottom row. All figures were done in time $t = 90\,\text{ps}$. The size of the system is $2000 \times 2000 \times 1$ of basis cells. Plotted with grid $= [100, 100, 1]$.

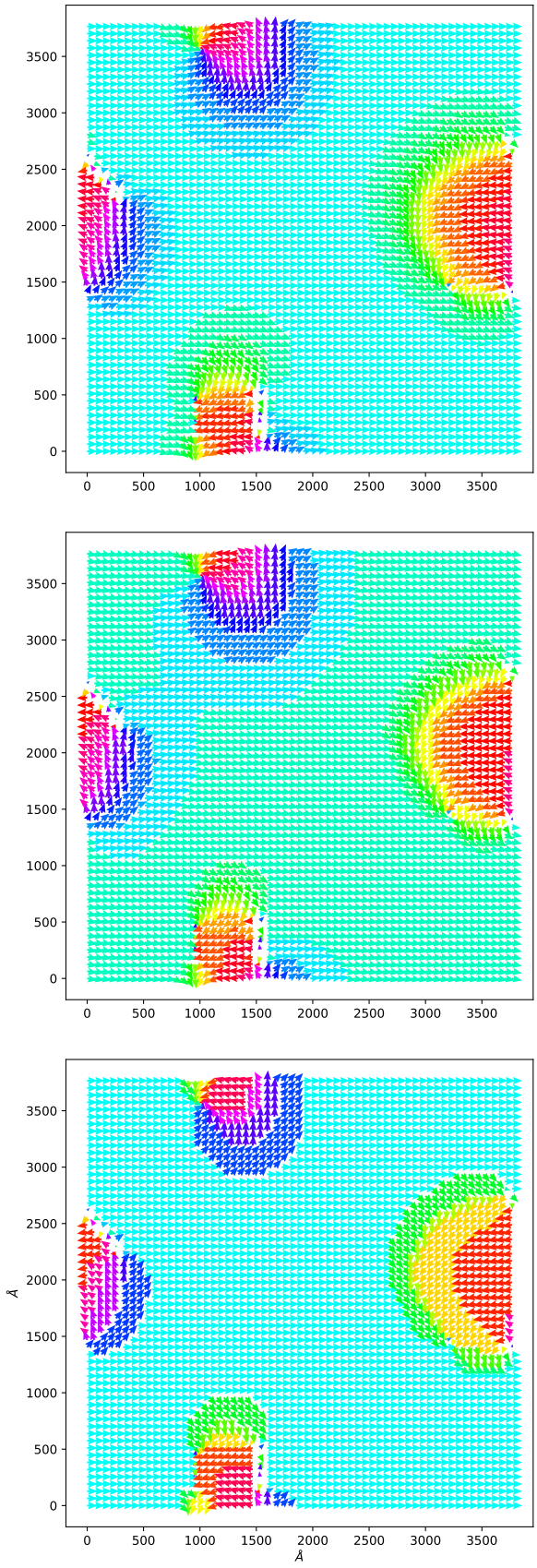

Figure 2.7: This figure was plotted using our above-mentioned algorithm, with $\epsilon = 0.3$ in the top row, $\epsilon = 0.5$ in the middle row, $\epsilon = 1$ in the bottom row, the figure was done in time $t = 100\,\text{ps}$. The size of the system is $1000 \times 1000 \times 1$ of basis cells. Plotted with grid $= [60, 60, 1]$.

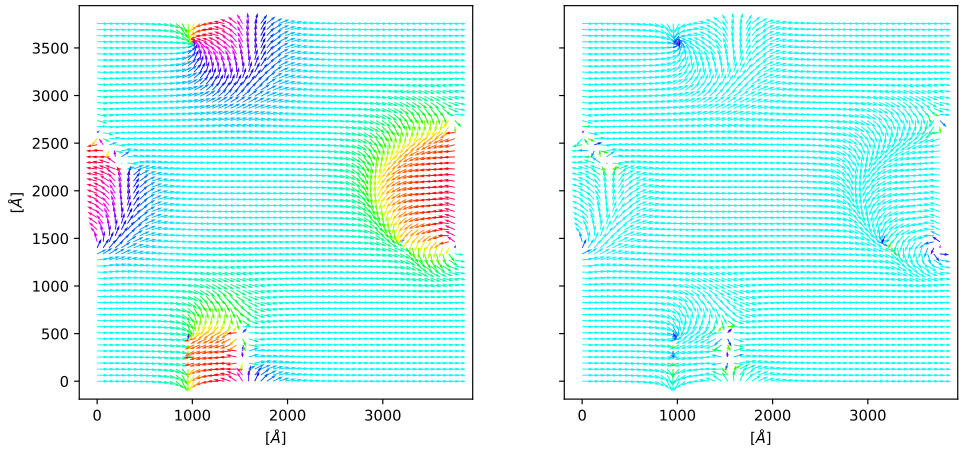

Figure 2.8: This was plotted using the script plot_L.py, figure was done in time $t = 100\,\mathrm{ps}$. The size of the system is $1000 \times 1000 \times 1$ of basis cells. Plotted with grid $= [60, 60, 1]$.

The figure depicts the same state of spins as Fig.2.7.

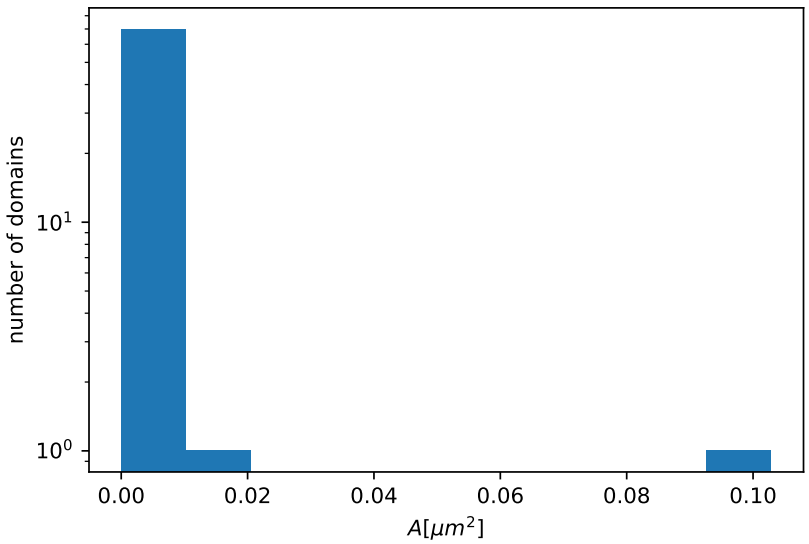

Figure 2.9: Histogram of the size of the domains, ten bins. The simulation captures the system in time $t = 100\,\mathrm{ps}$. The size of the system is $1000 \times 1000 \times 1$ of basis cells. Plotted with grid $= [60, 60, 1]$. On the x-axis, the area of each domain is plotted. The y-axis is logarithmic, as the number of small domains is very large.

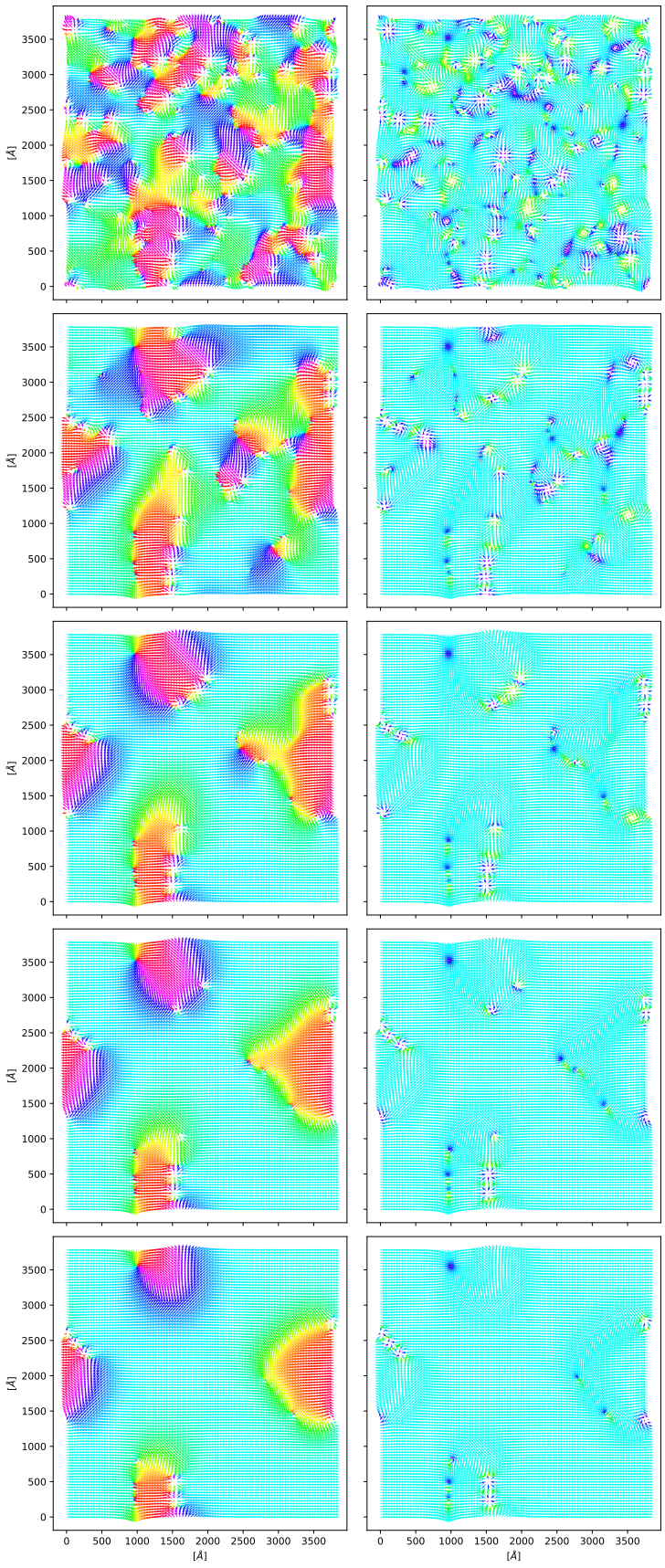

Figure 2.10: Time development of antiferromagnetic domains. In time from top row to bottom $t = 10\,\text{ps}$, $t = 30\,\text{ps}$, $t = 50\,\text{ps}$, $t = 70\,\text{ps}$, $t = 90\,\text{ps}$. Simulations were done with $T = 0\,\text{K}$ in a system of $1000 \times 1000 \times 1$ of basis cells. Plotted with grid $= [100, 100, 1]$.

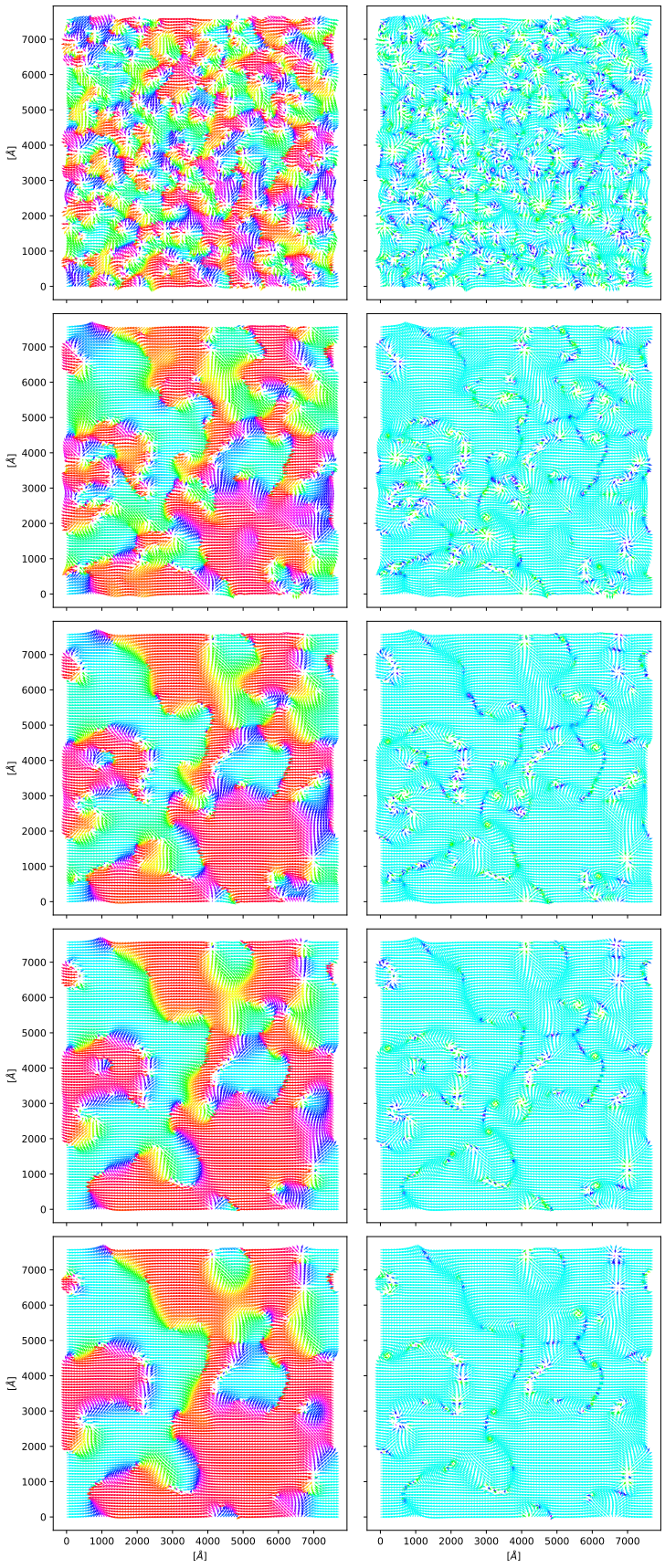

Figure 2.11: Time development of antiferromagnetic domains. In time from top row to bottom $t = 10\,\text{ps}$, $t = 30\,\text{ps}$, $t = 50\,\text{ps}$, $t = 70\,\text{ps}$, $t = 90\,\text{ps}$. Simulations were done with $T = 0\,\text{K}$ in a system with $2000 \times 2000 \times 1$ of basis cells. Plotted with grid $= [100, 100, 1]$.

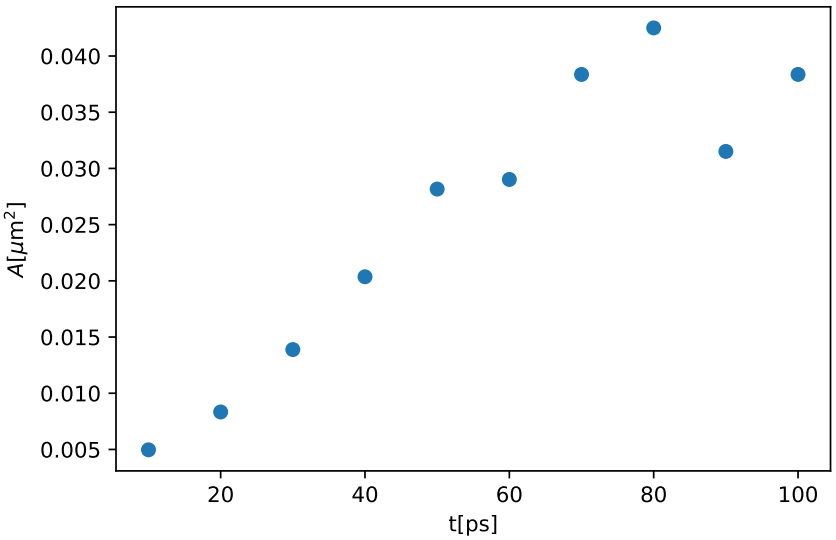

Figure 2.12: Figure shows the time dependence of the average size of magnetic domains. Only domains greater than $A_{\text{min}} = 4 \cdot 10^{-3}\,\mu\text{m}^2$ are considered. The simulations, which we plot, were done in a system of $1000 \times 1000 \times 1$ basis cells. The simulation was done with temperature $T = 0\,\text{K}$. The size of the domains was calculated using the algorithm for categorizing domains, whose functionality is pictured in Fig.2.7.

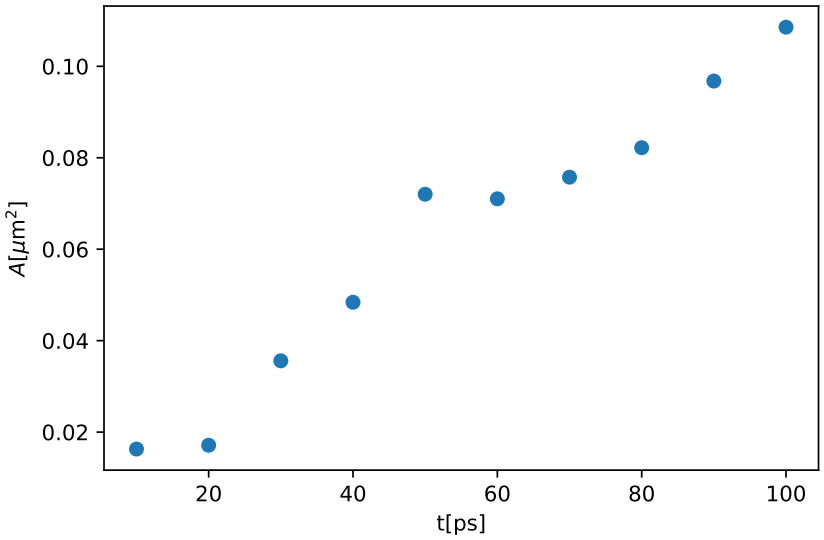

Figure 2.13: Figure shows the time dependence of the average size of magnetic domains. Only domains greater than $A_{\text{min}} = 4 \cdot 10^{-3}\,\mu\text{m}^2$ are considered. The simulations, which we plot, were done in a system of $2000 \times 2000 \times 1$ basis cells. The simulation was done with temperature $T = 0\,\text{K}$. The size of the domains was calculated using the algorithm for categorizing domains, whose functionality is pictured in Fig.2.7.

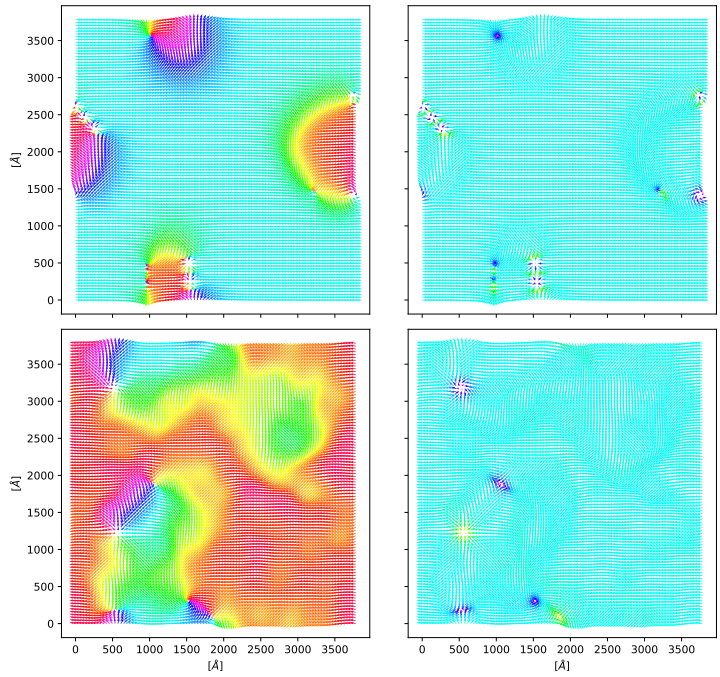

Figure 2.14: Simulation with $T = 0K$ (top row) and a simulation with $T = 200K$ (bottom row). Both figures were done in time $t = 100\,\text{ps}$. The size of the system is $1000 \times 1000 \times 1$ of basis cells. Plotted with grid $= [100, 100, 1]$

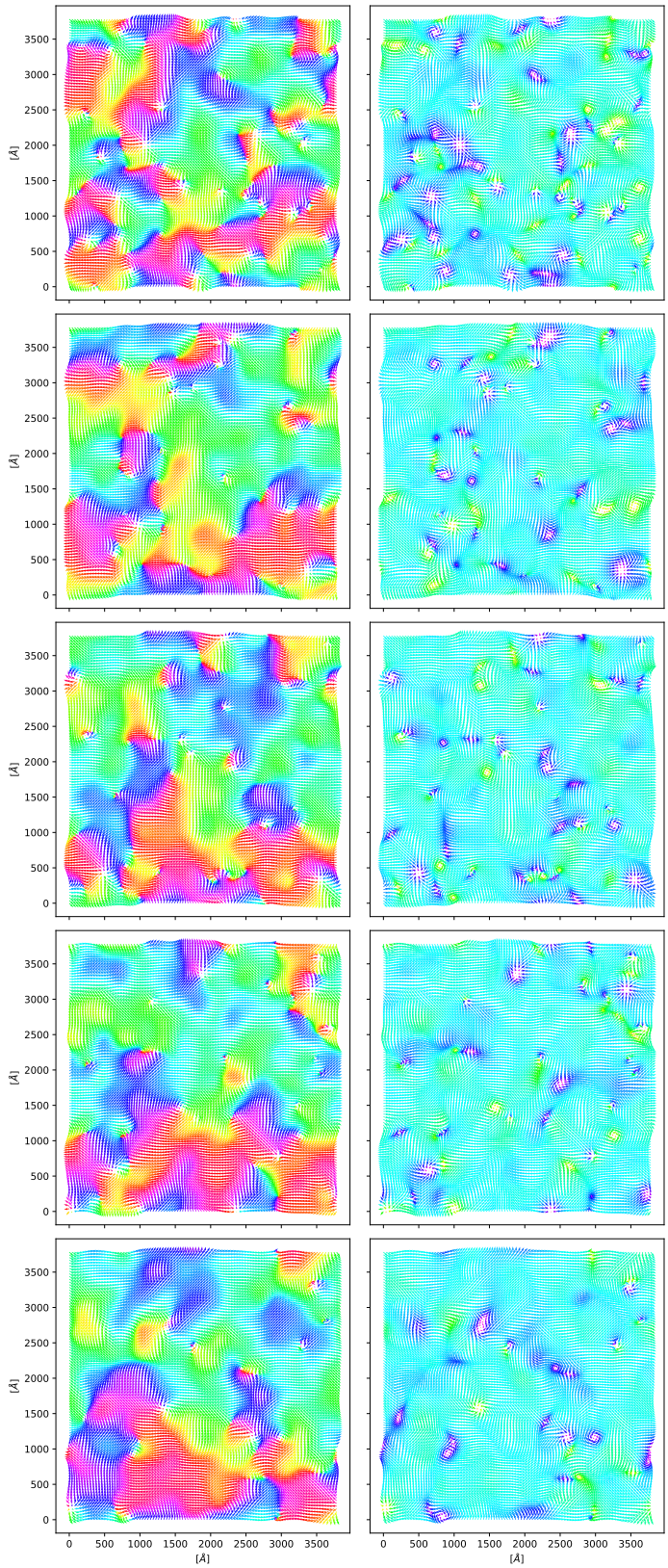

Figure 2.15: Time development of antiferromagnetic domains. In time from top row to bottom $t = 10\,\mathrm{ps}$, $t = 30\,\mathrm{ps}$, $t = 50\,\mathrm{ps}$, $t = 70\,\mathrm{ps}$, $t = 90\,\mathrm{ps}$. Simulations were done with $T = 300\,\mathrm{K}$ in a system with $1000 \times 1000 \times 1$ of basis cells. After that, the temperature of the system was changed to $T = 0\,\mathrm{K}$ and a simulation for $t_\mathrm{f} = 2\,\mathrm{ps}$ was run. Plotted with grid $= [100, 100, 1]$.

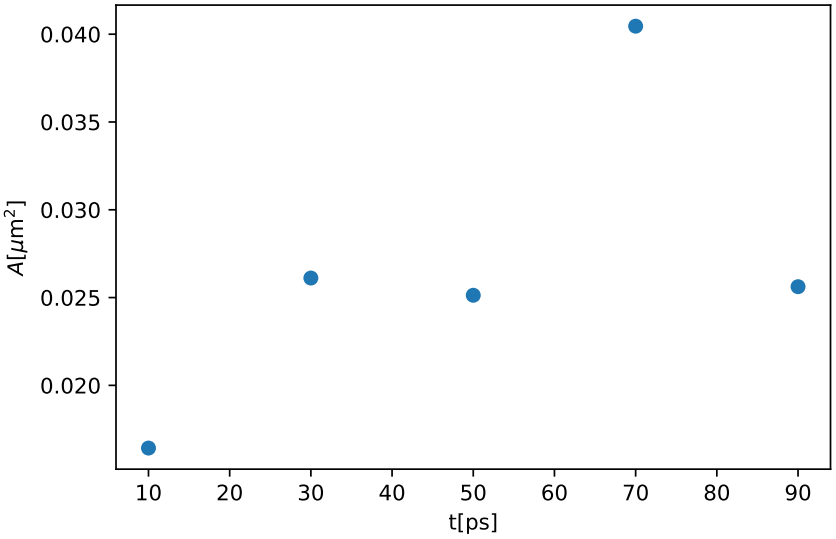

Figure 2.16: Figure shows the time dependence of the average size of magnetic domains. Only domains greater than $A_{\min} = 4 \cdot 10^{-3}\,\mu\mathrm{m}^2$ are considered. The simulations, which we plot, were done in a system of $1000 \times 1000 \times 1$ basis cells. The simulation was done with temperature $T = 300K$.

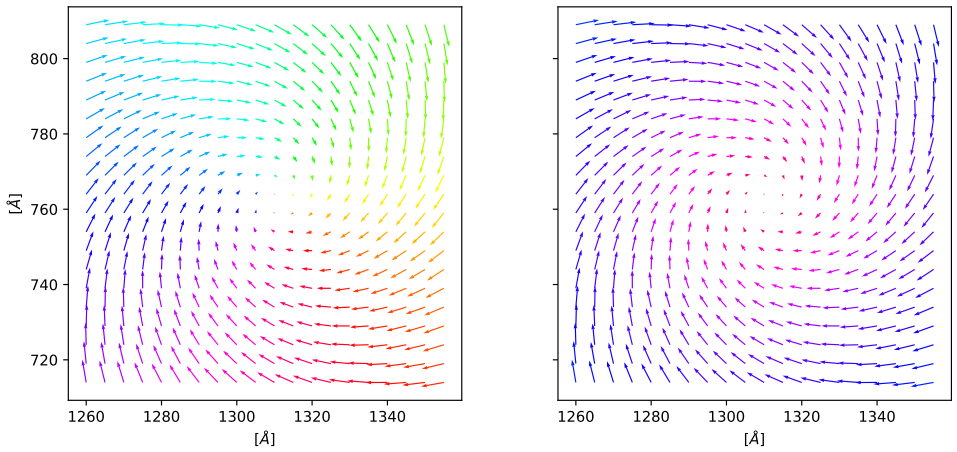

Figure 2.17: The Figure pictures a half-skyrmion.

Conclusion

In this work, atomistic simulations of the time development of spins were conducted, with the main goal of explaining the meta-stability of the broken-down domains in the CuMnAs quench-switching experiments. Firstly, the parameters of atomistic simulations were examined to determine their suitability for subsequent simulations. A time step of $\Delta t = 1$fs was deemed appropriate for the ensuing simulations. As the in-plane anisotropy constant and damping parameter are unknown, various values of the in-plane anisotropy constants and damping parameters were tested, leading to the choice of $K = 0.01$ and $\alpha = 0.1$, respectively. The simulations with zero temperature showed that the size of the domains grows in time. The average size of the domains was $d \simeq 100nm$ across. For a system of $2000 \times 2000 \times 1$, the domains were two times larger than those in a $1000 \times 1000 \times 1$ system. One of the objectives of this research was to explore the impact of non-zero temperature on the nano-fragmentation of antiferromagnetic domains. Preliminary results of the simulations conducted at room temperature indicated that the domains appeared considerably smaller than those observed in the zero-temperature system. Nevertheless, the dimensions of the domains were still significantly larger, approximately $d \simeq 100$nm across, in comparison to the findings obtained by [9], which demonstrated a nano-fragmented state of domains with dimensions of approximately $d \simeq 10$nm across. Moreover, the growth of the antiferromagnetic domains was observed on the ps timescale. In the experiments, domains retained the nano-fragmented state for $t \simeq$ s. This suggests that the observed metastability of nano-fragmented domains by Kaspar is a result of factors that are not accurately represented in the simulations. The average size of the domains was calculated by an algorithm, which was tested and verified to recognize antiferromagnetic domains successfully.

The non-zero temperature simulations showed dependence on the initial state of the spins and also on the size of the system. In spite of this, the results are qualitatively the same for all sizes of the system and the initial states. The system used in the simulations was $d \simeq 300-700nm$ in size, which is much smaller than the samples used in the experiments of [9]. To have a size of the system comparable to the experiment is unfeasible because of computational limitations.

As mentioned above, the finite temperature is not the cause of the nano-fragmentation of the domains. One possible reason for the discrepancy is the presence of crystal defects, such as interstitials and dislocations. These could be simulated by introducing a model with the pinning of some magnetic moments in a certain direction. The pinned magnetic moments would be insensitive to any interactions.

Bibliography

[1] O. J. Amin, S. F. Poole, S. Reimers, L. X. Barton, A. Dal Din, F. Maccherozzi, S. S. Dhesi, V. Novák, F. Krizek, J. S. Chauhan, R. P. Campion, A. W. Rushforth, T. Jungwirth, O. A. Tretiakov, K. W. Edmonds, and P. Wadley. Antiferromagnetic half-skyrmions electrically generated and controlled at room temperature. *Nature Nanotechnology*, 2023. doi: 10.1038/s41565-023-01386-3.

[2] H. B. Callen and Th. A. Welton. Irreversibility and Generalized Noise. *Phys. Rev.*, 83:34–40, 1951.

[3] C. L. Degen. Scanning magnetic field microscope with a diamond single-spin sensor. *Applied Physics Letters*, 92(24):243111, 2008.

[4] I. Fina, X. Marti, D. Yi, J. Liu, J. H. Chu, C. Rayan-Serrao, S. Suresha, A. B. Shick, J. Železný, T. Jungwirth, J. Fontcuberta, and R. Ramesh. Anisotropic magnetoresistance in an antiferromagnetic semiconductor. *Nature Commun.*, 5:4671, 2014.

[5] T.L. Gilbert. Classics in Magnetics A Phenomenological Theory of Damping in Ferromagnetic Materials. *IEEE Transactions on Magnetics*, 40(6):3443–3449, 2004.

[6] T. Hajiri, S. Ishino, K. Matsuura, and H. Asano. Electrical current switching of the noncollinear antiferromagnet Mn3GaN. *Applied Physics Letters*, 115 (5):052403, 2019.

[7] D. Jiles. *Introduction to Magnetism and Magnetic Materials*. Chapman and Hall, London, New York, 1991.

[8] M. Julliere. Tunneling between ferromagnetic films. *Physics Letters A*, 54 (3):225–226, 1975.

[9] Z. Kašpar, M. Surýnek, J. Zubáč, F. Krizek, V. Novák, R. P. Campion, M. S. Wörnle, P. Gambardella, X. Marti, P. Němec, K. W. Edmonds, S. Reimers, O. J. Amin, F. Maccherozzi, S. S. Dhesi, P. Wadley, J. Wunderlich, K. Olejník, and T. Jungwirth. Quenching of an antiferromagnet into high resistivity states using electrical or ultrashort optical pulses. *Nature Electronics*, 4(1):30–37, 2021.

[10] L.D. Landau and E.M. Lifshitz. On the theory of the dispersion of magnetic permeability in ferromagnetic bodies. *Phys. Z. Sowjetunion*, 8:153–164, 1935.

[11] J. H. Mentink, M. V. Tretyakov, A. Fasolino, M. I. Katsnelson, and Th. Rasing. Stable and fast semi-implicit integration of the stochastic Landau–Lifshitz equation. *Journal of Physics: Condensed Matter*, 22(17): 176001, 2010.

[12] G. P. Müller, M. Hoffmann, C. Dißelkamp, D. Schürhoff, S. Mavros, M. Sallermann, N. S. Kiselev, H. Jónsson, and S. Blügel. Spirit: Multifunctional framework for atomistic spin simulations. *Phys. Rev. B*, 99:224414, 2019.

[13] D.C. Ralph and M.D. Stiles. Spin transfer torques. *Journal of Magnetism and Magnetic Materials*, 320(7):1190–1216, 2008.

[14] C. F. Schippers, M. J. Grzybowski, K. Rubi, M. E. Bal, T. J. Kools, R. A. Duine, U. Zeitler, and H. J. M. Swagten. Disentangling electrical switching of antiferromagnetic NiO using high magnetic fields. *Phys. Rev. B*, 106: 174434, 2022.

[15] A. Scholl, J. Stöhr, J. Lüning, J. W. Seo, J. Fompeyrine, H. Siegwart, J.-P. Locquet, F. Nolting, S. Anders, E. E. Fullerton, M. R. Scheinfein, and H. A. Padmore. Observation of Antiferromagnetic Domains in Epitaxial Thin Films. *Science*, 287(5455):1014–1016, 2000.

[16] J. Železný, P. Wadley, K. Olejník, A. Hoffmann, and H. Ohno. Spin-transport, spin-torque and memory in antiferromagnetic devices. *Nature Phys.*, 14:220–228, 2018. doi: 10.1038/s41567-018-0062-7.

[17] P. Wadley, V. Hills, M. R. Shahedkhah, K. W. Edmonds, R. P. Campion, V. Novák, B. Ouladdiaf, D. Khalyavin, S. Langridge, V. Saidl, P. Nemec, A. W. Rushforth, B. L. Gallagher, S. S. Dhesi, F. Maccherozzi, J. Železný, and T. Jungwirth. Antiferromagnetic structure in tetragonal CuMnAs thin films. *Scientific Reports*, 5:17079, 2015.

[18] P. Wadley, B. Howells, J. Železný, C. Andrews, V. Hills, R. P. Campion, V. Novák, K. Olejník, F. Maccherozzi, S. S. Dhesi, S. Y. Martin, T. Wagner, J. Wunderlich, F. Freimuth, Y. Mokrousov, J. Kuneš, J. S. Chauhan, M. J. Grzybowski, A. W. Rushforth, K. W. Edmonds, B. L. Gallagher, and T. Jungwirth. Electrical switching of an antiferromagnet. *Science*, 351(6273): 587–590, 2016.

[19] P. Wadley, S. Reimers, M. J. Grzybowski, C. Andrews, M. Wang, J. S. Chauhan, B. L. Gallagher, R. P. Campion, K. W. Edmonds, S. S. Dhesi, F. Maccherozzi, V. Novak, J. Wunderlich, and T. Jungwirth. Current polarity-dependent manipulation of antiferromagnetic domains. *Nature Nanotechnology*, 13:362–365, 2018.

[20] M. S. Wörnle, P. Welter, Z. Kašpar, K. Olejník, V. Novák, R. P. Campion, P. Wadley, T. Jungwirth, C. L. Degen, and P. Gambardella. Current-induced fragmentation of antiferromagnetic domains. *arXiv:1912.05287*, 2019.

List of Figures